Nonlinear conductivity spectra of ionically conducting glasses and glass ceramics: Analysis of spectral shape and scaling properties

H. Staesche and B. Roling

Fachbereich Chemie, Philipps-Universität Marburg Hans-Meerwein-Strasse, 35032 Marburg, Germany

We present higher order conductivity spectra $\sigma_3'(\nu)$ of different ion conducting glasses and glass ceramics, which were taken over broad frequency ranges and at different temperatures. The $\sigma_3'(\nu)$ spectra are characterized by a change in sign, namely from positive values in the dc regime to negative values in the dispersive regime. In the dispersive regime, $\sigma_3'(\nu)$ exhibits an approximate power-law-type frequency dependence, albeit with a significantly larger exponent than the low-field conductivity $\sigma_1'(\nu)$. The $\sigma_3'(\nu)$ isotherms of an individual glass or glass ceramic can be superimposed by using the Summerfield scaling. The resulting $\sigma_3'(\nu)$ master curves of different materials show strong shifts on the scaled frequency axis with respect to each other. This implies strong differences between the materials regarding the nonlinearity of the dispersive conductivity. In order to rationalize this effect, we calculate the nonlinear dispersive hopping conductivity in a double-well potential approximation.

I. INTRODUCTION

The demand for improved energy storage has increased over the last years and will increase further in the future. One possible solution is electrochemical energy storage in batteries and supercapacitors.[1–6] Current research focuses on the enhancement of the energy and power densities of such devices. Since the achievable power density is influenced by the internal resistance of the cell, the solid or liquid electrolyte carrying the ionic current should have a low resistance. This can be realized by taking materials with a high specific ionic conductivity and by reducing the thickness of the electrolyte layer. For instance, in state-of-the-art lithium microbatteries, glassy electrolyte films with thicknesses in the range of $1-2$ μm are currently being used.[7,8] There are research efforts to further reduce the thickness into the 100 nm range.[9,10] In such thin films, the high electric field strength results in nonlinear ion transport, i.e., in a field dependence of the ionic conductivity. For instance, if a voltage of 3 V drops in a 100 nm electrolyte film, the electric field strength is 300 kV/cm. This clearly exceeds the upper limit for linear ion transport, which is in the range of 50–100 kV/cm. In the nonlinear regime, the current density j can be expressed by a power series of the electric field E

$$j = \sigma_1 \cdot E + \sigma_3 \cdot E^3 + \sigma_5 \cdot E^5 + \cdots. \quad (1)$$

Here, σ_1 denotes the low-field conductivity, while σ_3, σ_5, etc., are higher order conductivity coefficients. Equation (1) contains exclusively odd terms, since for isotropic ion conductors, the function $j(E)$ is odd. The nonlinearity has previously been studied using dc methods.[11–14] It was found that the effective dc conductivity $\sigma_{\mathrm{eff}} = j_{\mathrm{dc}}/E_{\mathrm{dc}} = \sigma_1 + \sigma_3 \cdot E_{\mathrm{dc}}^2 + \sigma_5 \cdot E_{\mathrm{dc}}^4 + \cdots$ increases with the field. This increase could lead to an improved performance of thin electrolytes. However, with dc methods it is difficult to distinguish between an intrinsic field dependence of the ion transport and Joule heating effects. Joule heating gives rise to an increase in temperature and could thus be responsible for the observed increase in conductivity. With ac impedance measurements it is

easier to distinguish between these effects. On the application of a sinusoidal field $E(t) = E_0 \sin(\omega t)$, Eq. (1) yields the following relation for the current density being in phase with the field:

$$
\begin{aligned}
j' ={}& \sigma_1' \cdot E_0 \sin(\omega t) + \sigma_3' \cdot E_0^3 \sin^3(\omega t) + \sigma_5' \cdot E_0^5 \sin^5(\omega t) + \cdots \\
={}& \sigma_1'(\omega) \cdot E_0 \sin(\omega t) + \frac{3}{4}\sigma_3'(\omega) \cdot E_0^3 \sin(\omega t) \\
&- \frac{1}{4}\sigma_3'(3\omega) \cdot E_0^3 \sin(3\omega t) + \frac{10}{16}\sigma_5'(\omega) \cdot E_0^5 \sin(\omega t) \\
&- \frac{5}{16}\sigma_5'(3\omega) \cdot E_0^5 \sin(3\omega t) + \frac{1}{16}\sigma_5'(5\omega) \cdot E_0^5 \sin(5\omega t) \\
&+ \cdots.
\end{aligned}
\quad (2)
$$

An equivalent equation can be derived for the current density being out of phase with the field.[15] As can be seen, the Fourier component at 3ω in Eq. (2) is related to the third-order term in Eq. (1), the 5ω component to the fifth-order term and so on. Joule heating increases the low-field conductivity $\sigma_1'(\nu)$ and produces also higher harmonic currents at 3ω. However, these 3ω currents are proportional to $(E_0)^2$ (Ref. 16) so that they can be clearly distinguished from the higher harmonic current term in Eq. (2). Consequently, the higher harmonic currents can be directly used to obtain the higher order conductivity coefficients σ_3', σ_5', etc.

The low-field conductivity spectra $\sigma_1'(\nu)$ of many solid electrolytes follow the time-temperature superposition principle, i.e., in a log-log representation the spectral shape of $\sigma_1'(\nu)$ is independent of temperature. At low frequencies, $\sigma_1'(\nu)$ displays a dc conductivity plateau with the value $\sigma_{1,\mathrm{dc}}$. This plateau reflects the long-range ion transport in the sample. Above an onset frequency ν_1^*, the low-field conductivity $\sigma_1'(\nu)$ becomes dispersive and increases with increasing frequency. This reflects subdiffusive ion transport, i.e., local hopping processes of the ions. In the dc regime and over the first decades of the dispersive regime, $\sigma_1'(\nu)$ can be

described, in a first approximation, by a Jonscher power law[17]

$$\sigma'_1(\nu) = \sigma_{1,dc}\left[1 + \left(\frac{\nu}{\nu_1^*}\right)^{p_1}\right] \tag{3}$$

with an exponent p_1, which is often in the range from 0.6–0.7.

The time-temperature superposition principle implies that the conductivity spectra taken at different temperatures can be superimposed by an appropriate scaling formalism, resulting in a conductivity master curve for a given electrolyte material. A common scaling formalism was established by Summerfield,[18,19] where $\sigma'_1(\nu)/\sigma_{1,dc}$ is plotted versus $\nu/(\sigma_{1,dc}\cdot T)$. The applicability of the Summerfield scaling for a given electrolyte material implies that the mean square displacement of the mobile ions at the crossover from subdiffusive to diffusive dynamics, $\langle r^2\rangle_{cr}$, is independent of temperature, thus pointing to a temperature-independent ion transport mechanism.[20] The Summerfield scaling can also be used to obtain information about different transport mechanisms in different materials. For instance, in the case of x $Na_2O(1-x)GeO_2$ glasses with variable Na_2O content x, it was found that the rms displacement at the crossover from subdiffusive to diffusive dynamics, $\sqrt{\langle r^2\rangle_{cr}}$ decreases from about 10 Å at $x=0.005$ to about 0.6 Å at $x=0.4$.[20] This huge difference in the spatial extent of the subdiffusive ion dynamics points to huge differences in the potential landscape of the mobile ions.

In this paper, we carry out, an analysis of the spectral shape of higher order conductivity spectra $\sigma'_3(\nu)$ of several ion conducting glasses and glass ceramics. To do this, we have measured the $\sigma'_3(\nu)$ spectra over broad frequency ranges and at different temperatures. We show that the $\sigma'_3(\nu)$ spectra of single alkali glasses are quite well described by a Jonscher-type power-law equation while the equation fails to describe the $\sigma'_3(\nu)$ spectra of mixed alkali glasses and of partially crystallized glass ceramics. Furthermore, we find that for a given material, Summerfield scaling leads to a superposition of the $\sigma'_3(\nu)$ spectra. Remarkably, when we compare the resulting Summerfield master curves of different materials, we find strong shifts between the master curves on the scaled frequency axis. These shifts are much stronger than found for the $\sigma'_1(\nu)$ Summerfield master curves. In order to rationalize this effect, we calculate the nonlinear dispersive conductivity due to hopping transport in a double-well potential approximation.

II. EXPERIMENTAL

For the nonlinear conductivity measurements, the following alkali alumino silicates and sodium germanates were prepared: $(Li_2O)_{1-x}(Na_2O)_xAl_2O_3(SiO_2)_4$ glasses with $x=0.1$ and 0.2 (LNASx); $Li_2OAl_2O_3(SiO_2)_2$ glass and glass ceramics with 6% and 13% crystallinity (LAS, amorphous, "am," and $x\%$ crystallinity) and a $(Na_2O)_{0.15}(GeO_2)_{0.85}$ glass (NG15). For the chemical formulas, the compositional parameter x is given in the range from 0 and 1, whereas for the abbreviations, x was multiplied by 100. The glasses were prepared by the melt quenching technique. For the alkali alumino silicates, appropriate mixtures of sodium carbonate, lithium carbonate, alumina, and silica were first heated to 1100 °C in order to decompose the carbonates and then heated to 1600 °C for 16 h before quenching the melt into a brass mold. The sodium germanate glass was prepared accordingly from a mixture of sodium carbonate and germania and quenched from 1400 °C. Chemicals of high purity were used in order to avoid an unintentional mixed alkali effect. However, we observed that the low-impurity level leads to an increased tendency for crystallization so that rapid cooling was important. Removal of stress caused by the quenching had to be carried out carefully: relaxation was achieved at temperatures 50–60 K below the glass transition temperature for at least 5 h and a cooling rate of 0.5 K/min. Crystallization of the LAS samples was carried out according to Ref. 21.

The glass samples were then cut into slices with an Accutom 5 (Struers). The desired thickness of the samples was obtained by high-precision lapping with a PM5 (Logitech). This way, thicknesses ranging from 80 to 200 μm were obtained. The glasses were then attached to the sample holder as described in Ref. 22. The liquid electrolyte was varied, depending on the temperature range of the measurement. At low temperatures from 223 to 303 K, a solution of lithium nitrate in a mixture of propylene carbonate and propylene glycol was used. At higher temperatures, these solvents start to evaporate, and thus a different electrolyte is required. Here, a saturated solution of sodium chloride in dried glycerol was used. Due to the relatively high glass transition temperature of glycerol, this electrolyte is, however, not suitable for measurements at low temperatures.

Impedance measurements were carried out with a Novocontrol Alpha-AK high-performance impedance analyzer equipped with a high voltage booster and a high-voltage interface. With the high voltage booster, ac voltages with a maximum amplitude of 2000 V (1414 V rms) can be applied. The sample temperature was controlled by the Novocontrol Quatro cryosystem.

III. RESULTS AND DISCUSSION

As described in Ref. 20, the higher order conductivity spectrum $\sigma'_3(\nu)$ can be determined by considering the Fourier components of the current density at 3ν in Eq. (2). Rearrangement yields

$$\frac{-4j'(3\nu)}{E_0} = \sigma'_3(\nu)\cdot E_0^2 + \frac{5}{4}\sigma'_5(3\nu)\cdot E_0^4 + \cdots. \tag{4}$$

For calculating σ'_3, the data were plotted in the form: $-4j'(3\nu)/E_0$ vs E_0^2. If contributions from the Fourier components at 5ν are small, the second term on the right-hand side of Eq. (4) is negligible, and the plot yields an approximately straight line with a slope of $\sigma'_3(\nu)$. This was indeed the case at low frequencies in the dc conductivity regime, see Fig. 1. At higher frequencies in the dispersive regime, a curvature in the plots was observed, see Fig. 1. Therefore, the data were fitted with a second-order polynomial, and σ'_3 was derived from the linear term.
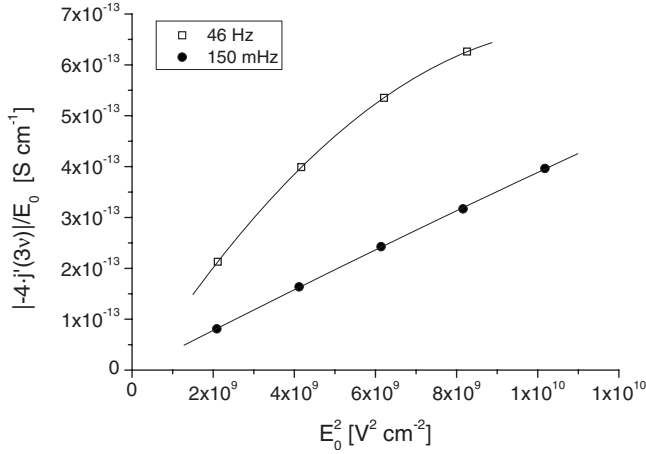
FIG. 1. Plot of $-4j(3\nu)/E_0$ vs E_0^2 for a LNAS20 glass at 273 K and different frequencies. The full circles denote positive values and the open squares negative values. Lines are second-order polynomial fits.
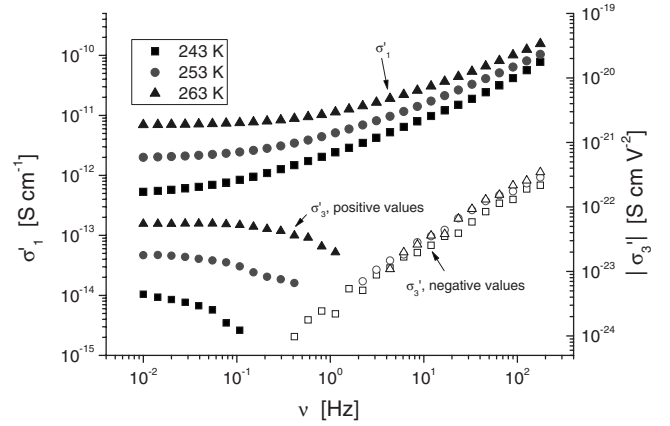

FIG. 2. Low-field conductivity spectra $\sigma_1'(\nu)$ and higher order conductivity spectra $|\sigma_3'(\nu)|$ of the mixed alkali glass LNAS20 at different temperatures; the applied field was 113 kV/cm; and empty symbols denote negative values and filled symbols positive values, respectively.

Typical isotherms of the low-field conductivity spectra $\sigma_1'(\nu)$ and of the third-order conductivity spectrum $\sigma_3'(\nu)$ for a LNAS20 glass sample are shown in Fig. 2. At low frequencies, both the $\sigma_1'(\nu)$ spectra and the $\sigma_3'(\nu)$ spectra are characterized by dc plateaus. At higher frequencies, the $\sigma_1'(\nu)$ spectra pass over in the well-known dispersive regime reflecting subdiffusive ion dynamics. In the same frequency range, $\sigma_3'(\nu)$ changes its sign from positive values in the dc regime to negative values in the dispersive regime. Consequently, in the log-log representation shown in Fig. 2, we have plotted the modulus of $\sigma_3'(\nu)$. In both the $\sigma_1'(\nu)$ spectra and the $\sigma_3'(\nu)$ spectra, the transition from the dc regime to the dispersive regime shifts to higher frequencies when the temperature is increased. Remarkably, the slope in the dispersive part of the $\sigma_3'(\nu)$ spectra, $p_3 = \frac{d\log|\sigma_3'(\nu)|}{d\log\nu} \approx 0.85-0.9$ is considerably larger than the slope in the dispersive part of the $\sigma_1'(\nu)$ spectra, $p_1 = \frac{d\log[\sigma_1'(\nu)]}{d\log\nu} \approx 0.7$.

These results indicate that both the $\sigma_1'(\nu)$ spectra and the $\sigma_3'(\nu)$ spectra reflect bulk ion transport. Interfacial effects,

i.e., ion blocking at the solid/liquid electrolyte interface, do not seem to have a significant influence on these spectra. As we have discussed in Ref. 15, such interfacial effects can be observed in the nonlinear capacitance spectra of solid ion conductors. This is, however, not the subject of the present paper.

For a further analysis, we tried to fit the $\sigma_3'(\nu)$ spectra with a Jonscher-type power-law expression

$$\sigma_3'(\nu) = \sigma_{3,\mathrm{dc}}\left[1 - \left(\frac{\nu}{\nu_3^*}\right)^{p_3}\right] \qquad (5)$$

with an exponent p_3. Note that in this expression, the frequency-dependent part is negative, accounting for the negative values of $\sigma_3'(\nu)$ in the dispersive regime. We found that the $\sigma_3'(\nu)$ spectra of single alkali glasses are quite well fitted by Eq. (5), see Fig. 3(a) as an example. Less well fitted are mixed alkali glasses and partially crystallized LAS glass ceramics, see Fig. 3(b). The reason for this is unclear at
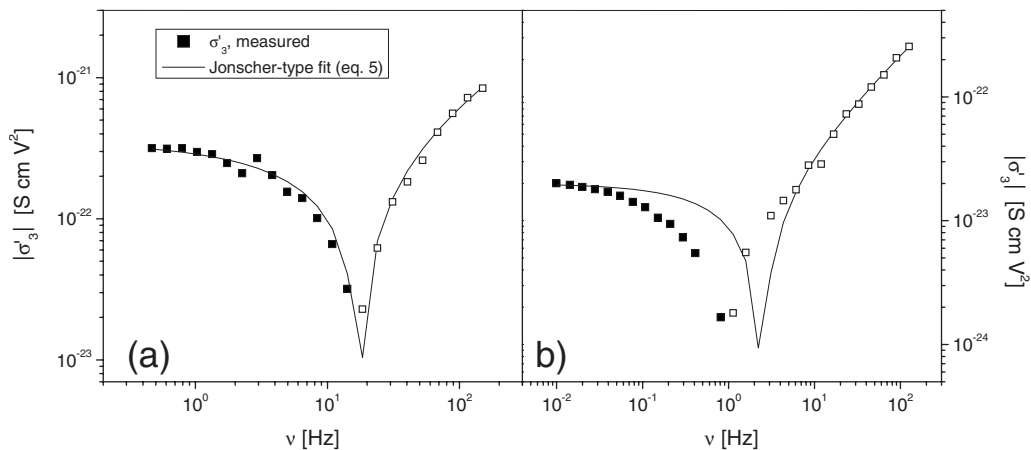

FIG. 3. Higher order conductivity spectra $|\sigma_3'(\nu)|$ of: (a) the LAS, am glass at 273 K and (b) LAS, 13% cryst. glass ceramic at 253 K; filled symbols correspond to positive values and empty symbols to negative values, respectively; and the solid line denote fits with the Jonscher-type power-law expression in Eq. (5).
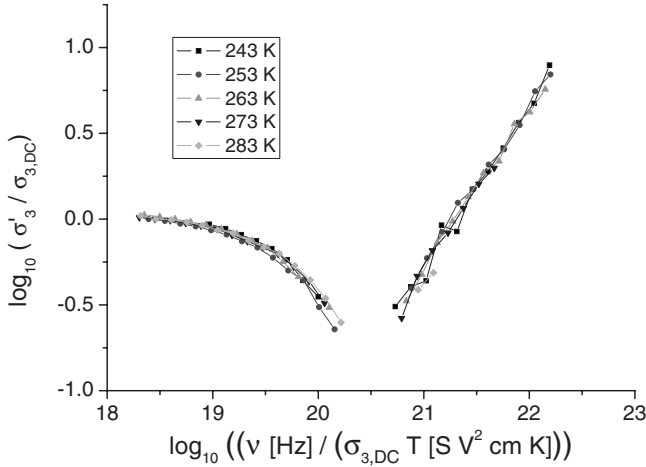
FIG. 4. Summerfield plot of the higher-order conductivity spectra $\sigma_3'(\nu)$ of the LNAS20 glass.

present. Comparison to hopping models should yield more insight.[23]

The spectral shape of $\sigma_3'(\nu)$ appears to be similar at different temperatures. Therefore, the question arises as to whether the $\sigma_3'(\nu)$ spectra obey the time-temperature superposition principle and can be superimposed by an appropriate scaling formalism. In Fig. 4, we show a Summerfield plot of the conductivity isotherms of the LNAS20 glass, i.e., a plot of $\sigma_3'(\nu)/\sigma_{3,\mathrm{dc}}$ versus $\nu/(\sigma_{3,\mathrm{dc}} \cdot T)$. The third-order dc conductivity $\sigma_{3,\mathrm{dc}}$ was determined from third-order complex impedance plots.[15] The errors in the $\sigma_3'(\nu)$ spectra are, in general, larger than in the $\sigma_1'(\nu)$ spectra, especially close to the change in sign, where the modulus $|\sigma_3'(\nu)|$ becomes very small. Therefore, the scaled $\sigma_3'(\nu)$ spectra in Fig. 4 exhibit more scatter than the scaled $\sigma_1'(\nu)$ spectra of the same glass. However, for a given material and within the experimental error, we observe no systematic deviations from superposition of the scaled $\sigma_3'(\nu)$ isotherms. This was found for all

glasses and glass ceramics so that we could generate Summerfield master curves for the individual materials.

In Fig. 5, we show the $\sigma_3'(\nu)$ master curves for different materials (right-hand side) and we plot in comparison the $\sigma_1'(\nu)$ master curves of the same materials (left-hand side). The master curves of the low-field conductivity $\sigma_1'(\nu)$ show only weak shifts on the scaled frequency axis. In comparison, the master plots of the higher order conductivity $\sigma_3'(\nu)$ show much stronger shifts on the $\nu/(\sigma_{3,\mathrm{dc}} \cdot T)$ axis. Since the ratios $\sigma_{3,\mathrm{dc}}/\sigma_{1,\mathrm{dc}}$ are similar for all materials, a shift of the $\sigma_3'(\nu)$ master curve to higher $\nu/(\sigma_{3,\mathrm{dc}} \cdot T)$ values implies a *weaker nonlinearity* of the dispersive conductivity. Thus, the NG glass exhibits the strongest nonlinearity of the dispersive conductivity, while the mixed alkali glasses LNAS10 and LNAS20 exhibit the weakest nonlinearity. Partial crystallization of the LAS glass leads to a weaker nonlinearity.

In the following, we will address mainly two questions: (i) why is $\sigma_3'(\nu)$ negative in the dispersive regime? (ii) Why do some materials show a weaker nonlinearity in the dispersive regime than others?

We note that negative values for $\sigma_3'(\nu)$ in the dispersive regime have been observed in computer simulations of hopping models.[23] However, the origin of the negative values has not been clarified up to now. Since a general theory for the higher order conductivity $\sigma_3'(\nu)$ does not yet exist, we start with the simplest approximation for the description of the dispersive hopping conductivity in disordered materials, that is, hopping in double-well potentials (DWP) as sketched in Fig. 6. We will first calculate the nonlinearity of the conductivity in a symmetrical double well potential [Fig. 6(a)] and then in a strongly asymmetric double-well potential [Fig. 6(b)]. We will show that the asymmetry of the double-well potential exhibits a strong influence on the nonlinearity of the dispersive conductivity. This is relevant for our disordered materials since the potential landscape of the mobile ions should be characterized by a broad distribution of site energies.
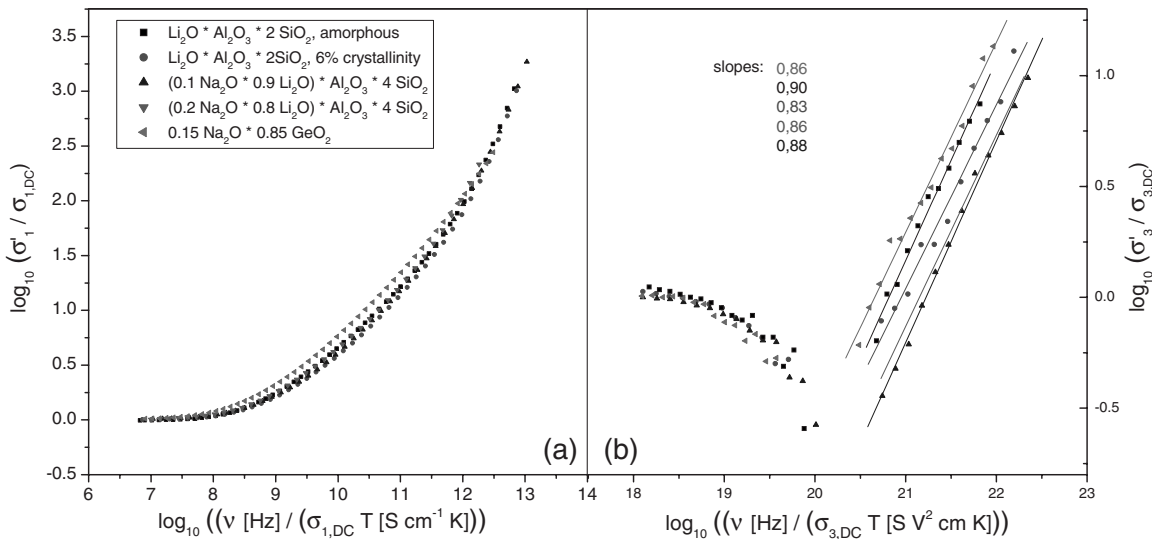

FIG. 5. Summerfield master curves of different glasses and glass ceramics; same symbols correspond to the same material; (a) master curves of the low-field conductivity spectra $\sigma_1'(\nu)$ and (b) master curves of the higher order conductivity spectra $\sigma_3'(\nu)$ (solid lines correspond to linear fits of the scaled data in the dispersive regime).
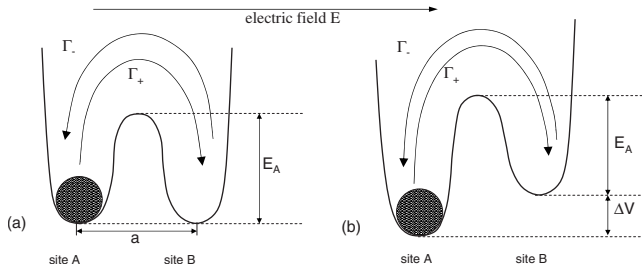
FIG. 6. Hopping dynamics of an ion in the presence of an electric field (a) in a symmetric double-well potential and (b) in an asymmetric double-well potential; Γ_+ is the hopping rate in the direction of the field, and Γ_- the hopping rate in the opposite direction; E_a is the barrier height, ΔV the site energy difference and a the hopping distance.

The calculation of the nonlinear conductivity in the double-well potentials will be done in the time domain under the influence of a constant electric field. On short time scales, only few uncorrelated hops take place. In a frequency-domain experiment, this corresponds to the high-frequency plateau regime,[24,25] which is not accessible in our experiments. On longer time scales, the ion current drops and eventually a constant electrical polarization is achieved. This corresponds to the dispersive conductivity regime in our frequency-domain experiments.

We start with the symmetric double-well potential with two ion sites A and B. After switching on an electric field E at time 0, we can write down the following master equation for the time-dependent probability $W_B(t)$ to find an ion at site B

$$\frac{dW_B(t)}{dt} = \Gamma_+ - (\Gamma_+ + \Gamma_-)W_B(t) \qquad (6)$$

with $\Gamma_+(t) = \Gamma \exp(\frac{qaE}{2kT})$ and $\Gamma_-(t) = \Gamma \exp(-\frac{qaE}{2kT})$ denoting the hopping rate of the ion in field direction and against field direction, respectively. Γ is the hopping rate without field, q is the charge of the ion and a is the hopping distance (distance between the sites).

The differential equation can be solved with the following ansatz:

$$W_B(t) = C + D \exp(-t/\tau). \qquad (7)$$

Inserting this ansatz into Eq. (6) yields

$$1/\tau = \Gamma_+ + \Gamma_- = 2\Gamma \cosh(u),$$

$$C = \frac{\Gamma_+}{\Gamma_+ + \Gamma_-} \quad \text{and} \quad D = 0.5 - C = -\tanh(u) \qquad (8)$$

with $u = \frac{qaE}{2kT}$.

Without field, the center of ionic charge is at $x = 0$. In the limit of very large fields, the probability to find the ions at site B approaches unity, corresponding to a dipole moment of $qa/2$. Thus, the polarization in the long-time limit can be written as
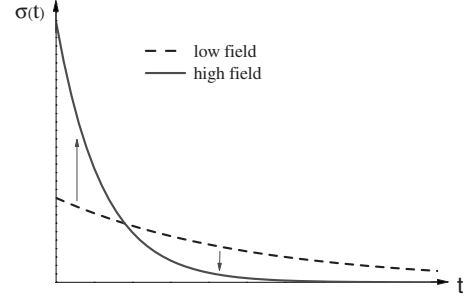

FIG. 7. Schematic illustration of the time-dependent effective conductivity $\sigma(t)$ in a symmetric double-well potential at different field strengths; the dashed line represents the effective conductivity at low fields while the solid line represents the effective conductivity at higher fields.

$$P_\infty = \frac{1}{3}N_V q \frac{a}{2}[W(t \to \infty) - W(t = 0)] = \frac{1}{3}N_V q \frac{a}{2}(-D)$$

$$= \frac{1}{6}N_V qa \tanh(u). \qquad (9)$$

On the other hand, the current density in the short-time limit is given by

$$j_0 = \frac{1}{3}N_V q \frac{a}{2} \lim_{t \to 0}\left[\frac{dW_B(t)}{dt}\right] = \frac{1}{3}N_V q \frac{a}{2}(-D)\frac{1}{\tau}$$

$$= \frac{1}{3}N_V qa\Gamma \sinh(u) \qquad (10)$$

Now we consider the field dependence of the quantities in Eqs. (8)–(10). The $\sinh(u)$ function in Eq. (10) implies that the short-time current density j_0 increases with the field in a *superlinear* fashion: $\sinh(u) = u + \frac{1}{6}u^3 + \cdots$. Thus, the effective short-time conductivity $\sigma_0 \equiv \frac{j_0}{E} \propto 1 + \frac{1}{3}u^2$ increases with the field. On the other hand, the relaxation time τ decreases with increasing field according to: $1/\tau = 2\Gamma \cosh(u) = 2\Gamma(1 + \frac{1}{2}u^2 + \cdots)$. This is illustrated schematically in Fig. 7. Due to the faster temporal drop of the current density at higher fields, the long-time polarization increases with increasing field in a *sublinear* fashion: $P_\infty \propto \tanh(u) = u - \frac{1}{3}u^3 + \cdots$. The time-dependent current density can be written as

$$j(t) = \frac{1}{3}N_V q \frac{a}{2}\frac{dW_B(t)}{dt} = \frac{1}{3}N_V q \frac{a}{2}(-D)\frac{1}{\tau}\exp(-t/\tau)$$

$$= \frac{1}{3}N_V qa\Gamma\left(u + \frac{1}{6}u^3 + \cdots\right)\exp(-2\Gamma t)\exp(-\Gamma u^2 t)\ldots. \qquad (11)$$

The term $\exp(-\Gamma u^2 t)$ leads to a sublinear increase in the current density with the field on time scales $t \gg 1/\Gamma$. Thus, on these time scales, the effective conductivity $\sigma(t \gg 1/\Gamma) = j(t \gg 1/\Gamma)/E$ decreases with increasing field, as sketched in Fig. 7. In a frequency-domain experiment, this corresponds to a decrease of $\sigma_1'(\nu)$ with increasing field and to negative $\sigma_3'(\nu)$ values in the dispersive regime.

Next, we consider an *asymmetric* double-well potential as shown in Fig. 6(b). The asymmetry is characterized by the
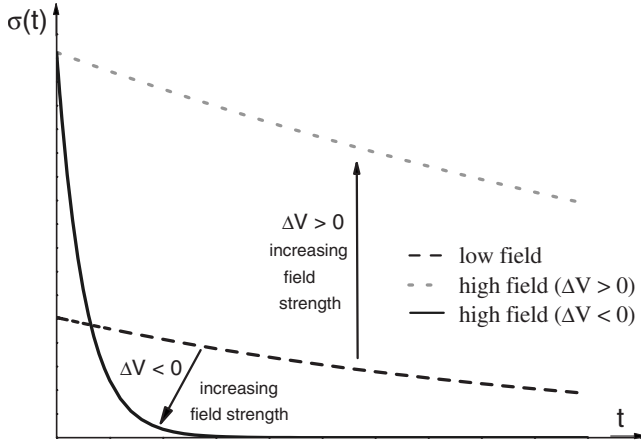
FIG. 8. Schematic illustration of the time-dependent effective conductivity $\sigma(t)$ in a strongly asymmetric double-well potential; the dashed line represents the effective low-field conductivity, the dotted line the high-field effective conductivity for $\Delta V > 0$, and the full line the high-field effective conductivity for $\Delta V < 0$, respectively.

difference between the potential energies of sites A and B relative to the thermal energy, $\Delta V/kT$. Now, it is important to differentiate between two cases: (i) $\Delta V > 0$, i.e., site A has a lower potential minimum than site B and (ii) $\Delta V < 0$, where site B has the lower potential minimum.

In case (i) $\Delta V > 0$, we define the jump rates as $\Gamma_+(t) = \Gamma \exp(-\frac{\Delta V}{kT})\exp(u)$ and $\Gamma_-(t) = \Gamma \exp(-u)$. Using the same procedure as for the symmetric case we obtain the following expression for the inverse relaxation time $1/\tau$:

$$1/\tau = \Gamma_+ + \Gamma_- = \Gamma\left[\exp\left(-\frac{\Delta V}{kT}\right)\exp(u) + \exp(-u)\right]$$
$$\approx \Gamma \exp(-u). \tag{12}$$

The approximation in Eq. (12) holds for strong asymmetries $\Delta V \gg kT$. In this case, the long-time polarization P_∞ and the short-time current density j_0 are given by

$$P_\infty = \frac{1}{6}N_V qa \exp(-\Delta V/kT)[\exp(2u) - 1],$$

$$j_0 = \frac{1}{3}N_V qa\Gamma \exp(-\Delta V/kT)\sinh(u). \tag{13}$$

Equations (12) and (13) imply that both the short-time current and the long-time polarization increase with increasing field and that the decay of $j(t)$ becomes slower with increasing field. Thus, in contrast to the symmetric DWP, the current density $j(t)$ increases superlinearly with increasing field on all time scales, as illustrated in Fig. 8. Furthermore, it is important to note that the factor $\exp(-\Delta V/kT)$ implies smaller current densities and polarizations than in the symmetric DWP.

In case (ii) $\Delta V < 0$, we define the jump rates as $\Gamma_+(t) = \Gamma \exp(u)$ and $\Gamma_-(t) = \Gamma \exp(-\frac{|\Delta V|}{kT})\exp(-u)$. This results in

$$1/\tau = \Gamma_+ + \Gamma_- = \Gamma\left[\exp(u) + \exp\left(-\frac{|\Delta V|}{kT}\right)\exp(-u)\right]$$
$$\approx \Gamma \exp(u),$$

$$P_\infty = \frac{1}{6}N_V qa \exp(-|\Delta V|/kT)[1 - \exp(-2u)],$$

$$j_0 = \frac{1}{3}N_V qa\Gamma \exp(-|\Delta V|/kT)\sinh(u). \tag{14}$$

The short-time current is identical to case (i), however in contrast to case (i), the exponential decay of $j(t)$ becomes faster with increasing field, see Fig. 8. This results in a decrease of the long-time current density $j(t \gg 1/\Gamma)$ with increasing field.

In a disordered potential landscape, one has to average over the cases (i) and (ii). This implies that the current density on longer time scales $t \gg 1/\Gamma$ is determined by case (i). Thus, the averaged long-time effective conductivity increases with increasing field. In addition, we have to average over the distribution of site energies leading to a distribution of $|\Delta V|$ values in the DWP approximation. When $\Delta V = 0$, the long-time effective conductivity $\sigma(t \gg 1/\Gamma)$ is *large* and *decreases* with increasing field. When $|\Delta V| \gg kT$, the long-time effective conductivity $\sigma(t \gg 1/\Gamma)$ is much *smaller*, but it *increases* with increasing field. Thus, we expect that the averaged effective conductivity $\langle\sigma(t \gg 1/\Gamma)\rangle$ is determined by small ΔV values and that accordingly, $\langle\sigma(t \gg 1/\Gamma)\rangle$ decreases with increasing field. An increase of the width of the $|\Delta V|$ distribution leads to (a) lower values for the averaged effective conductivity $\langle\sigma(t \gg 1/\Gamma)\rangle$ and (b) to a less pronounced decrease in $\langle\sigma(t \gg 1/\Gamma)\rangle$ with increasing field. In a frequency-domain experiment, a broader distribution of ΔV values should therefore lead to a weaker nonlinearity in the dispersive conductivity. Thus, our experimental results suggest that the potential landscape in the single alkali glass NG15 is characterized by the narrowest distribution of site energies while the site energy distribution is broadest in the mixed alkali glasses LNAS10 and LNAS20. Partial crystallization of the LAS glass leads to a broadening of the site energy distribution.

Finally, we note that the present results for the nonlinear dispersive conductivity obtained in the framework of a double-well potential approximation should be compared to results obtained in computer simulations of the nonlinear ion dynamics in disordered potential landscapes. This will give valuable insights into the range of applicability of the DWP approximation for calculating nonlinear conductivity spectra. Furthermore, it would be interesting to correlate the present results for the nonlinear conductivity to other properties related to ion dynamics, in particular, to deviations of the linear dc conductivity from Arrhenius behavior and to features in the nearly constant loss (NCL) observed at low temperatures and/or high frequencies.[26–29] It has been predicted theoretically that a distribution of ion site energies produces a curvature in Arrhenius plots of the linear dc conductivity[30] and that the asymmetry of DWPs influences the NCL.[26,27] In the present study, the temperature range is too narrow for a

meaningful analysis of the curvature. Measurements in the NCL regime were not possible since very high frequencies and/or low temperatures cannot be realized with our special experimental setup. Therefore, additional low-field conductivity measurements on the same glasses and glass ceramics with ion-blocking metal electrodes will be necessary.

IV. CONCLUSIONS

We have measured nonlinear conductivity spectra of different glasses and glass ceramics over broad frequency ranges and at different temperatures. At low frequencies, the higher order conductivity $\sigma'_3(\nu)$ is positive and exhibits a dc plateau regime. At higher frequencies, there is a transition into a dispersive regime where $\sigma'_3(\nu)$ becomes negative. In the dispersive regime, $\sigma'_3(\nu)$ exhibits an approximate power-law-type frequency dependence, however with a significantly larger exponent $p_3 = \frac{d \log |\sigma'_3(\nu)|}{d \log \nu} \approx 0.85 - 0.9$ than found for the low-field spectra, $p_1 = \frac{d \log \sigma'_1}{d \log \nu} \approx 0.7$. The $\sigma'_3(\nu)$ spectra of single alkali glasses are well described by a Jonscher-type power-law equation while this equation fails to describe the $\sigma'_3(\nu)$ spectra of mixed alkali glasses and of partially crystallized glass ceramics.

The $\sigma'_3(\nu)$ spectra of all glasses and glass ceramics obey the time-temperature superposition principle. Therefore, the $\sigma'_3(\nu)$ isotherms of an individual material could be superimposed by using the Summerfield scaling approach. The resulting $\sigma'_3(\nu)$ master curves of different materials were found to exhibit a strong shift with respect to each other on the scaled frequency axis. Remarkably, this shift is much stronger than for the $\sigma'_1(\nu)$ master curves of the same materials. This implies strong differences between these materials regarding the nonlinearity of the dispersive conductivity. A calculation of the nonlinear dispersive conductivity of hopping ions in a double-well potential approximation suggests that the origin of this effect is closely related to the distribution of ionic site energies.

[1] A. Chandra, A. J. Roberts, E. L. H. Yee, and R. C. T. Slade, Pure Appl. Chem. **81**, 1489 (2009).

[2] H. S. Chen, T. N. Cong, W. Yang, C. Q. Tan, Y. L. Li, and Y. L. Ding, Prog. Nat. Sci. **19**, 291 (2009).

[3] E. Meissner and G. Richter, J. Power Sources **116**, 79 (2003).

[4] T. Noda, S. Kato, Y. Yoshihisa, K. Takeuchi, and K. Murata, J. Power Sources **43**, 89 (1993).

[5] M. D. Ingram, H. Staesche, and K. S. Ryder, J. Power Sources **129**, 107 (2004).

[6] B. E. Conway, V. Birss, and J. Wojtowicz, J. Power Sources **66**, 1 (1997).

[7] P. Vinatier and Y. Hamon, in *Charge Transport in Disordered Solids*, edited by S. Baranovski (Wiley, New York, 2006).

[8] K. H. Joo, P. Vinatier, B. Pecquenard, A. Levasseur, and H. J. Sohn, Solid State Ionics **160**, 51 (2003).

[9] http://www.hicondelec.com/

[10] F. Berkemeier, M. R. S. Abouzari, and G. Schmitz, Ionics **15**, 241 (2009).

[11] J. Vermeer, Physica (Amsterdam) **22**, 1257 (1956).

[12] J. P. Lacharme and J. O. Isard, J. Non-Cryst. Solids **27**, 381 (1978).

[13] J. M. Hyde and M. Tomozawa, Phys. Chem. Glasses **27**, 147 (1986).

[14] J. L. Barton, J. Non-Cryst. Solids **203**, 280 (1996).

[15] H. Staesche, S. Murugavel, and B. Roling, Z. Phys. Chem. **223**, 1229 (2009).

[16] C. Crauste-Thibierge, C. Brun, F. Ladieu, D. L'Hote, G. Biroli, and J.-P. Bouchaud, arXiv:1002.0498 (unpublished).

[17] A. K. Jonscher, Nature (London) **267**, 673 (1977).

[18] S. Summerfield, Philos. Mag. B **52**, 9 (1985).

[19] S. Summerfield and P. N. Butcher, J. Non-Cryst. Solids **77-78**, 135 (1985).

[20] B. Roling, C. Martiny, and S. Bruckner, Phys. Rev. B **63**, 214203 (2001).

[21] R. M. Biefeld, G. E. Pike, and R. T. Johnson, Phys. Rev. B **15**, 5912 (1977).

[22] S. Murugavel and B. Roling, J. Non-Cryst. Solids **351**, 2819 (2005).

[23] B. Roling, S. Murugavel, A. Heuer, L. Luhning, R. Friedrich, and S. Rothel, Phys. Chem. Chem. Phys. **10**, 4211 (2008).

[24] K. Funke, Defect Diffus. Forum **143-147**, 1243 (1997).

[25] K. Funke, C. Cramer, and B. Roling, Glass Sci. Technol. (Offenbach, Ger.) **73**, 244 (2000).

[26] X. Lu and H. Jain, J. Phys. Chem. Solids **55**, 1433 (1994).

[27] X. Lu, H. Jain, and O. Kanert, J. Non-Cryst. Solids **172-174**, 1436 (1994).

[28] B. Roling, C. Martiny, and S. Murugavel, Phys. Rev. Lett. **87**, 085901 (2001).

[29] D. L. Sidebottom and M. Bassett, Z. Phys. Chem. **223**, 1161 (2009).

[30] K. W. Kehr, K. Massawisade, G. M. Schütz, and T. Wichmann, in *Diffusion in Condensed Matter*, edited by P. Heitjans and J. Kärger (Springer-Verlag, Berlin, 2005).